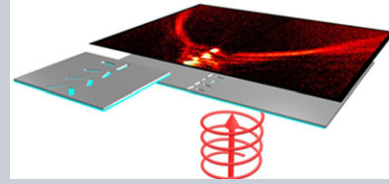


Abstract Since the surface plasmon polariton (SPP) has received a great deal of attention because of its capability of guiding light within the subwavelength scale, finding methods for arbitrary SPP field generation has been a significant issue in the area of integrated optics. To achieve such a goal, it will be necessary to generate a plasmonic complex field. In this paper, we propose a novel method for generating a plasmonic complex field propagating with arbitrary curvatures by using double-lined distributed nanoslits. As a unit cell, two facing nanoslits are used for tuning both the amplitude and the phase of excited

SPPs as a function of their tilted angles. For verification of the proposed design rule, the authors experimentally demonstrate some plasmonic caustic curves and Airy plasmons.



A double-lined metasurface for plasmonic complex-field generation

Eui-Young Song^{1,**}, Seung-Yeol Lee^{1,**}, Jongwoo Hong¹, Kyoookun Lee¹, Yohan Lee¹, Gun-Yeal Lee¹, Hwi Kim², and ByoungHo Lee^{1,*}

1. Introduction

In the field of nanophotonics, methods for manipulating optical waves within the subwavelength scale have attracted great interest. One possible way to achieve highly confined optical waves beyond the diffraction limit would be the use of surface plasmon polaritons (SPPs), which are electromagnetic surface waves formed by collective oscillations of photons and electrons on the surface of a conductor [1–3]. Therefore, the spatial control of both the amplitude and phase of an SPP wave is considered to be a very important issue. Such a complex modulation of an SPP field makes it possible to realize the perfect generation of an arbitrary SPP wavefront profile, and such a capability would lead to innovative technologies in many fields of optical science and engineering such as optical trapping [4, 5], the routing of SPP energy along particular trajectories [6–13], next-generation optical holography [14, 15], and biosensing [16, 17].

While spatial light modulators (SLMs) are the most popular choice for complex-field modulation in free space, an alternate strategy is needed for the control of SPPs. For this reason, various methods for manipulating the wavefront of an SPP have been proposed in recent years. Plasmonic vortices introducing a geometrical phase shift by shaping curved slits [18–21], binary modulated gratings using a holographic method for beam shaping [7, 22–24], graded-index methods for modifying optical paths [25–27], and manipulating SPP propagation using periodic scatterers [10, 28–30] are some examples of these efforts. However, to the best of our knowledge, most of these methods are

phase-only types or are only applicable to special cases [9, 12].

On the other hand, a metasurface has recently emerged as one of the most powerful methods for controlling the amplitude and the phase profile of light in free space [31–34]. A metasurface is often defined as an artificially designed two-dimensional structure that is composed of arrays of subwavelength-size unit cells. The unit cells of metasurfaces interact with the incident light that results in changes in the optical properties of the incident light. Given the fact that metasurfaces can be employed to manipulate light in free space, these design principles were also applied for manipulating the phase of SPPs by using nanoslit arrays. Columns of slanted nanoslits provide polarization-controlled tunable directional coupling that facilitates both the bidirectional and unidirectional launching of SPPs [35]. Single or double arrays of nanoslits with a specific tilted-angle distribution, which can switch the direction and length of focus by tuning polarization, have also been proposed [36]. Similar concepts were applied to a plasmonic vortex lens consisting of circularly distributed nanoslits [37, 38]. In addition, a method for the polarization-multiplexing of SPP phase profiles has been proposed [39]. Very recently, several research groups have reported on the generation of various plasmonic fields [9, 24, 30]. For example, Airy plasmons were generated by an engineered nanoscale phase grating [9], but this methodology cannot be applied to arbitrary beam shaping because the grating is only applicable for expressing a binary amplitude change. On the contrary, in reference [30], plasmonic caustic beams, bottle beams, and a switchable dual foci lens were generated by

¹ National Creative Research Center for Active Plasmonics Application Systems, Inter University Semiconductor Research Center and School of Electrical Engineering, Seoul National University, Seoul 151–744, Korea

² Department of Electronics and Information Engineering, Korea University, 2511 Sejong-ro, Sejong 339–700, Korea

**These authors are equally contributed to this work.

*Corresponding Author: E-mail: byoungHo@snu.ac.kr

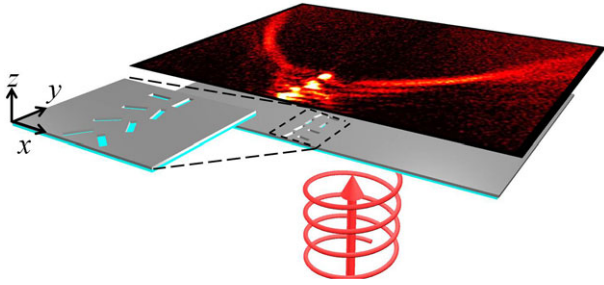


Figure 1 Schematic diagram of the proposed complex SPP field-generation device.

arranging chains of nanoantennas. However, this method only manipulates the phase of the SPPs, therefore it cannot be applied to complex-field generation such as Airy beams or cosine-Gaussian beams.

In this paper, a novel method for generating a plasmonic complex field propagating with arbitrary curvatures is proposed. To accomplish this, we used double-lined distributed nanoslit arrays in which each nanoslit has its own tilted angle. Both the amplitude and phase of the generated SPP can be independently controlled by tuning the tilted angles of the nanoslits. Therefore, with the backside illumination of left circularly polarized (LCP) light or right circularly polarized (RCP) light, the proposed double-lined distributed nanoslits can generate arbitrary complex SPP fields. As proof of concept, caustic waves and Airy plasmons were generated. Although a method for the complete control of the amplitude and phase of SPPs has been presented by introducing a new class of plasmonic holograms [24], our work can be distinguished from this work because our method introduces a novel double-lined distributed nanoslits configuration that is more compact and has the potential for beam tunability by adjusting the incident polarization and incident angle.

The manuscript is organized as follows. The design principle of the proposed structure is explained in Section 2. As proof of concept, we show two examples of the generation of arbitrary SPP fields. In Section 3, we demonstrate the generation of plasmonic caustic waves that have an arbitrary designed line curvature as a phase-only type example. For the example of full complex-field generation, an Airy plasmon, which requires both a gradually changing amplitude and a discrete changing profile, is also demonstrated in Section 4. Finally, a conclusion of the findings is shown in Section 5.

2. Distributed nanoslits for plasmonic complex-field generation

A schematic diagram of the proposed structure for complex SPP field generation is shown in Fig. 1. The structure is composed of arrays of subwavelength-scale nanoslit segments on a thin metal film. These nanoslits are double-lined with a constant period along the longitudinal axis (y -axis). In addition, each nanoslit has its own tilted angle along the

longitudinal axis, thus permitting both the amplitude and phase of SPPs launched from the nanoslit arrays to be controlled with respect to the normal incidence of circularly polarized light. Before we examine the characteristics of SPP excitation from the proposed double-lined distributed nanoslits, let us start with a more fundamental geometry – a single-lined nanoslit array.

2.1. SPP excitation characteristics from single-lined nanoslit array

Although SPP excitation characteristics from a single-lined nanoslit array with a constant tilted angle have already been analyzed in [36], we would like to briefly mention it again for a clear understanding of the proposed structure. If the period of the slit is shorter than the effective wavelength of the SPP (λ_{SPP}), a plane-wave SPP field is generated on the normal illumination of circularly polarized light. The amplitude (A) and phase (Φ) profile of the launched SPP propagating in the $+x$ -direction can be approximated as follows [36]:

$$A(\theta) = A_0 |\cos(\theta)|, \quad (1)$$

$$\Phi(\theta) = \pm \left(\theta - \pi u \left(\theta - \frac{\pi}{2} \right) \right). \quad (2)$$

The plus and minus signs of Eq. (2) correspond to the cases of LCP and RCP incidence, respectively, and the function u indicates the unit step function. In Eqs. (1) and (2), only one degree of freedom (ϑ) can be controlled; therefore it is not possible to fully implement a complex field. To independently modulate the amplitude and phase of the SPP wave, there needs to be at least two degrees of freedom in designing a complex-field-generation device, which will be introduced in the next section.

2.2. SPP excitation characteristics from double-lined nanoslit arrays

We now propose double-lined distributed nanoslits that have two degrees of freedom (ϑ_L and ϑ_R), as shown in Fig. 2a. The range of the generated plasmonic complex field can be calculated by using Eqs. (1) and (2). These two equations can be rewritten in a more compact form as $A(\vartheta)e^{j\Phi(\vartheta)} = \cos(\vartheta)e^{\pm j\vartheta}$. If we define the complex amplitude of the SPP field propagating along the $+x$ -direction generated by the right(left)-side array of nanoslits as $a_{R|+x}$ ($a_{L|+x}$), the interference of these two fields can be expressed as,

$$\begin{aligned} a_{R|+x} + a_{L|+x} \\ = \cos(\vartheta_R)e^{\pm j\vartheta_R} + \cos(\vartheta_L)e^{\pm j\vartheta_L}e^{jk_{\text{SPP}}D}, \end{aligned} \quad (3)$$

where ϑ_R (ϑ_L) is the tilted angle of right(left)-side nanoslit, k_{SPP} is the wave number of SPP, and the plus and minus

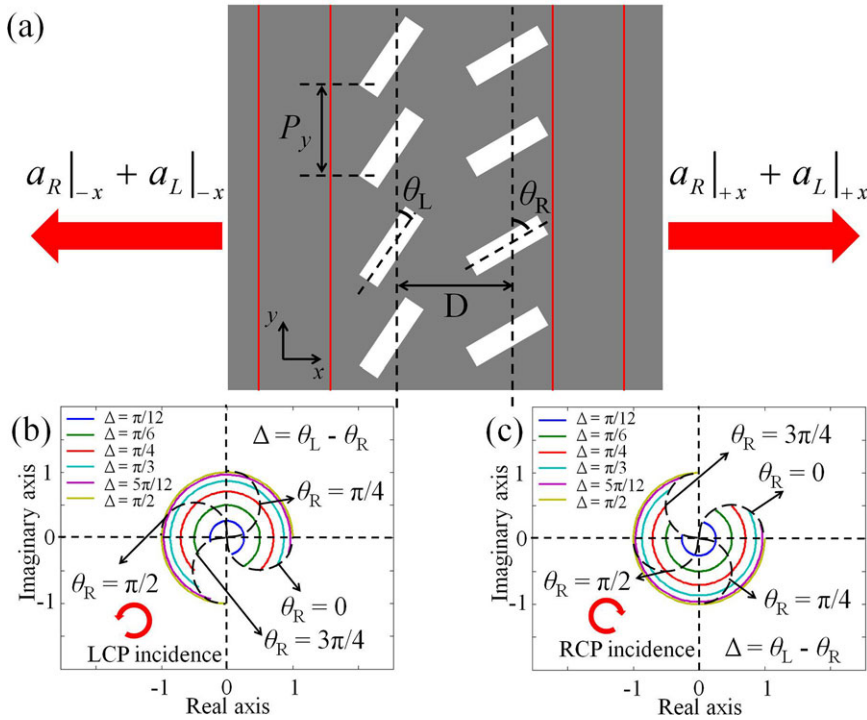


Figure 2 (a) Schematic diagram of double-lined distributed nanoslits with constant tilted angles of θ_L and θ_R . The period of the nanoslit segments is P_y . Red lines represent the propagation of SPP. For (b) LCP incidence and (c) RCP incidence, the range of complex-field modulation is plotted when θ_R is changed from 0 to $3\pi/4$. The x - and y -axes represent the real and imaginary values for the complex amplitude of the SPP field generated from the proposed double-lined distributed nanoslits.

signs of Eq. (3) correspond to the cases of LCP and RCP incidences, respectively. Throughout this paper, the distance between two lines is given by $D = \lambda_{\text{SPP}}/2$. Therefore the phase difference between left- and right-side lines caused by the geometrical distance is always π in our configuration. By substituting $e^{jk_{\text{SPP}}D} = -1$, we can rearrange Eq. (3) as,

$$a_R|_{+x} + a_L|_{+x} = \frac{1}{2} (1 - e^{\pm j2(\theta_L - \theta_R)}) e^{\pm j2\theta_R}. \quad (4)$$

According to Eq. (4), the amplitude of the SPP can be modeled as the angular difference between two nanoslits ($\Delta = \theta_L - \theta_R$), whereas the phase is controlled by the offset rotation angle (θ_R). Equation (4) is plotted in Fig. 2b for LCP incidence and in Fig. 2c for RCP incidence where the θ_R is changed from 0 to $3\pi/4$. It is clearly shown that a different amplitude (radius of circle) can be achieved with a different value of Δ . If the θ_R is changed from 0 to π , the unit circle of the complex plane can be completely filled, which means that the full range of the complex field can be covered. This facilitates arbitrary complex-field generation if we consider the two slits located at the same y -axis as a unit pixel. It is noteworthy that a SPP field propagating along the $-x$ -direction can also be expressed as,

$$a_R|_{-x} + a_L|_{-x} = -\frac{1}{2} (1 - e^{\pm j2(\theta_L - \theta_R)}) e^{\pm j2\theta_R}, \quad (5)$$

which has equal magnitude and opposite sign compared with Eq. (4).

2.3. Design of nanoslit distribution

We now describe the workflow of the proposed method. We initially set the desired plasmonic complex-field profile (such as caustics or Airy beam profile) to be generated. Because the SPP sources are excited from the array of discrete nanoslits, it is necessary to sample the complex-field profile. However, there are various points to be considered in determining the sampling period. First, the sampling period must be shorter than the operating wavelength to avoid unwanted interference of each source. It has been shown that such unwanted interference generates multiple beams [36]. On the other hand, the lower limit of the sampling period is determined by the dimension of the nanoslit to avoid the attachment of neighboring two nanoslits. Two factors should be considered in determining the dimension of nanoslits: one is the desired power for generating SPPs, and the other is the resolution limit in fabrication.

In the subwavelength scale, in general, larger slit dimensions guarantee a stronger excitation of SPPs; therefore the proposed structure may have a high efficiency for larger slit dimensions. On the other hand, smaller slit dimensions ensure a shorter sampling period that guarantees a high resolution. However, the lower limit of slit dimensions is restricted by the desired power of the generated SPPs. Therefore, it should be noted that there is a trade-off relation between coupling efficiency and sampling resolution of the proposed structure. Moreover, the aspect ratio of the rectangular nanoslit should be carefully designed because a nanoslit with a sufficiently high aspect ratio can only maintain the high polarization sensitivity of SPP excitation characteristics.

After determining the appropriate dimension of the nanoslit and the sampling period with the abovementioned criteria, ϑ_L and ϑ_R are determined by using Fig. 2b or 2c according to the type of circular polarization. Finally, we obtain the appropriate shape of the nanoslit array for plasmonic complex-field generation. As long as the restricted slit size is realistic in fabrication, it is possible to generate an arbitrary plasmonic complex field with the proposed workflow.

3. A phase-only example: Arbitrary SPP curve profile via caustics

In order to verify the abovementioned method, we need to generate an SPP curve profile via caustics. The generation of an arbitrary convex wave via caustics is a well-established method as evidenced by literature references [7, 23, 40]. If the desired analytical curve is $y = f(x)$, the corresponding spatial phase function $\varphi(y)$ at the line $x = 0$ can be calculated. The caustic curve $f(x)$ can be generated by the family of virtual geometrical tangent rays drawn by connecting each point in $y = f(x)$ with the corresponding point in $x = 0$. If the tangent of the slope is defined by ϑ_t , the relation between the spatial phase function $\varphi(y)$ at the line $x = 0$ and caustic curve $y = f(x)$ is expressed as [40],

$$\frac{d\varphi(y)}{dy} = k_{SPP} \sin \theta_t = \frac{k_{SPP} f'(x)}{\sqrt{1 + [f'(x)]^2}}, \quad (6)$$

where k_{SPP} is the wave number of the SPP mode. By using Eq. (6), $\varphi(y)$ can be calculated from $f(x)$. In our double-lined nanoslit array configuration, we set the location of the right-line nanoslit array as the reference line $x = 0$.

3.1. Design of plasmonic caustic curve

The following three analytical curves: $y_1 = a_1 x^{1.5}$, $y_2 = a_2 x^2$, and $y_3 = a_3 x^{2.5}$ where $a_1 = 5.0 \times 10^{-2}$, $a_2 = 1.7 \times 10^{-2}$, and $a_3 = 4.3 \times 10^{-3}$ (in micrometer units), respectively, are generated. Using Eq. (6), we can obtain the spatial phase function $\varphi(y)$ at the line $x = 0$. The amplitude profiles of these caustic curves are constant along y . Therefore, we only need to sample the phase profile $\varphi(y)$. The phase profiles $\varphi(y)$ of the three curves and the sampled points are shown in Fig. 3a. The sampling range is from $y = -18 \mu\text{m}$ to $y = 0 \mu\text{m}$ for curves y_1 and y_2 . For curve y_3 , the sampling range is from $y = -30 \mu\text{m}$ to $y = 0 \mu\text{m}$. These ranges are identical to each of the total length of the nanoslit array in the numerical simulations and experimental results. The number of each sample is $n_1 = 61$, $n_2 = 61$, and $n_3 = 101$ for curves $y_1 = a_1 x^{1.5}$, $y_2 = a_2 x^2$, and $y_3 = a_3 x^{2.5}$, respectively. Hence, the period of sampling is 300 nm over all curves, and a slit dimension of $260 \text{ nm} \times 80 \text{ nm}$ is used. The coupling efficiency is defined

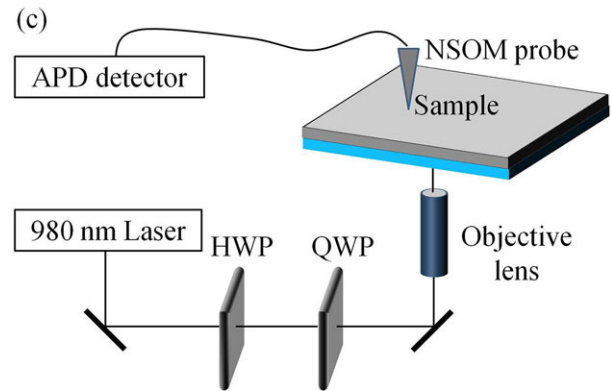
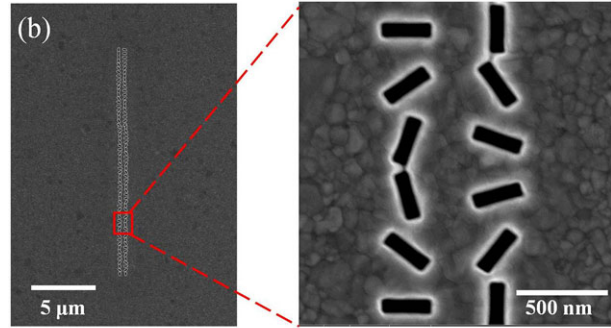
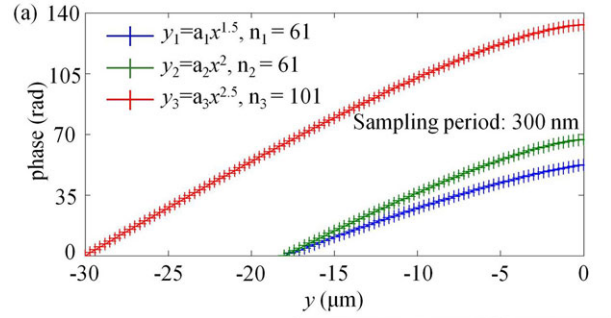


Figure 3 The phase profiles $\varphi(y)$ and their sampling locations for $y_1 = a_1 x^{1.5}$, $y_2 = a_2 x^2$, and $y_3 = a_3 x^{2.5}$. Sampling locations are marked as '+' (b) FE-SEM images of fabricated sample for $y_2 = a_2 x^2$. (c) Experimental setup for near-field scanning of the proposed structure. The laser source with a free space wavelength of 980 nm illuminates the bottom of the sample with circular polarization.

as the power of an integrated SPP at $x = 3 \mu\text{m}$ divided by the total incident power passing through the opened area of the double-lined nanoslit array. The efficiency of coupling from free-space to the SPPs wave for a $260 \text{ nm} \times 80 \text{ nm}$ slit dimension is calculated to be $\sim 7\%$. In this section, we select the polarization as LCP. Based on a table of the relation between a complex field and the tilted angle shown in Fig. 2b, we determined appropriate tilted angles, ϑ_L and ϑ_R along the y -axis. Because the intended caustic curves need only phase modulation, we selected $\vartheta_L - \vartheta_R = \pi/2$, which guarantees the maximum power of the generated SPP. This condition corresponds to the largest circle in Fig. 2b. In this unit circle, we can find appropriate ϑ_L and ϑ_R corresponding to the phase of the designed field.

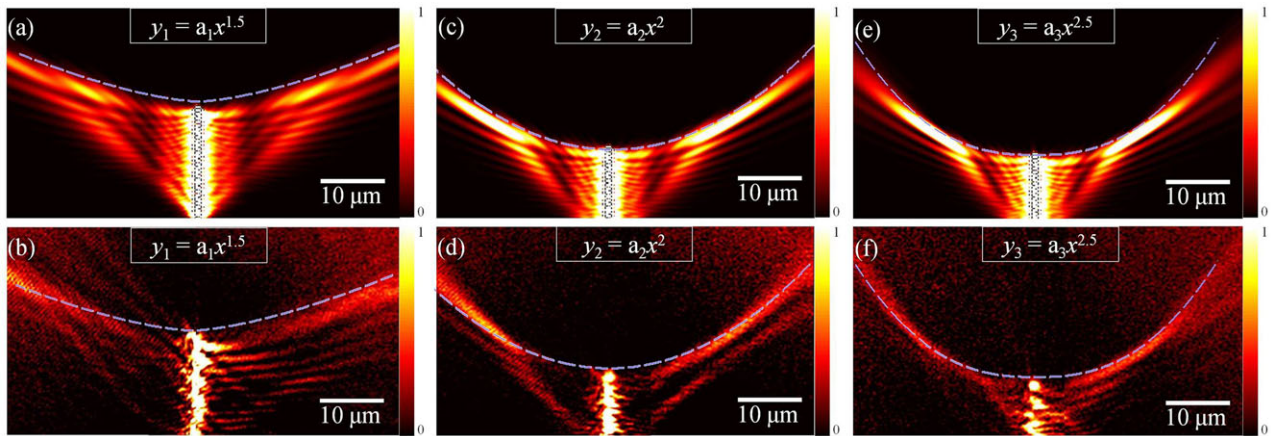


Figure 4 Numerical simulations and experimental results for the following analytical caustics curves: $y_1 = a_1 x^{1.5}$ for (a) simulation and (b) NSOM image. $y_2 = a_2 x^2$ for (c) simulation and (d) NSOM image. $y_3 = a_3 x^{2.5}$ for (e) simulation and (f) NSOM image. Blue dashed curves are the target curves $y = f(x)$.

3.2. Simulation and experimental results

To verify the validity of the aforementioned design process, we provide some experimental results with numerical simulations. For sample fabrication, an Ag layer with a thickness of 200 nm was evaporated on a fused silica wafer (MUHAN, MHS-1800). Then each slit patterns were inscribed on the Ag layer using a focused ion beam (FIB) (FEI, Helios 650). Figure 3b shows the field-enhanced scanning electron microscope (FE-SEM) images of the fabricated sample for curve $y_2 = a_2 x^2$. According to the right-side image with a higher magnification, it is possible to confirm that the size of the fabricated nanoslit is smaller than the sampling period. The sample was then illuminated from the bottom by a laser with the free-space wavelength of 980 nm and the generated SPP field-intensity distribution was measured by near-field scanning optical microscopy (NSOM) (Nanonics, Multi-view 4000). We scanned a region of $33 \mu\text{m} \times 33 \mu\text{m}$ at once (the maximum limit of our system) divided into 128×128 pixels with a duration time of 64 ms for each pixel. The experimental setup is shown in Fig. 3c. Due to the large size of the generated caustics beam (more than $33 \mu\text{m}$ in the x -direction), each NSOM image shown in Fig. 4 is a merged image of two NSOM measurement results.

To simulate the intensity distribution of the generated plasmonic complex field, we employed a finite-difference time-domain (FDTD) analysis. The experimental results and the numerical simulations for the three curves are presented in Fig. 4. Simulation results of the three curves are in good agreement with the blue dashed curves, which are the target curves $y = f(x)$. In addition, the symmetrical shape of the generated field intensity from the double-lined nanoslit array can be confirmed analytically, as shown in Eqs. (4) and (5). Small deviations from the blue dashed curves in Figs. 4c and e are evident. We conclude that this small mismatch originates from the finite length of double-lined nanoslit array. This restricts the range of the SPP curves that exactly follow the blue dashed curves.

Experimental results for the three curves also show some deviation from the blue dashed lines, showing a slightly asymmetric shape of the generated field intensity. We believe that such asymmetry occurs because the incident light is not strictly normal to the sample. A more detailed discussion concerning the influence of the oblique incident light can be found in the supplementary material (Part A). The finite numerical aperture of the objective lens in the experimental setup might also play a role that causes the intensity of the incident light and the incidence angle to be nonuniform. These asymmetric deviations can be reduced by improving the overall alignment of the experiment setup.

4. A Complex-field example: Generation of plasmonic Airy beam

4.1. Design of plasmonic Airy beam

The previous section dealt with the phase-only modulation of a plasmonic field. In this section, we intend to manipulate the example that needs both amplitude and phase control. For this purpose, we choose the appropriate example as a plasmonic Airy beam, which will be generated by a procedure similar to that in the previous section.

The envelope of the Airy packet represents an oscillating function with alternating positive maxima and negative minima. Therefore, the phase distribution of the Airy function shows alternating segments with values of 0 and π , which needs the simultaneous design of both the amplitude and phase. The complex-field profile of the Airy plasmon can be expressed as [9]

$$f(y) = \text{Airy} \left(\frac{y}{y_0} \right) \exp \left(a \frac{y}{y_0} \right) \quad (7)$$

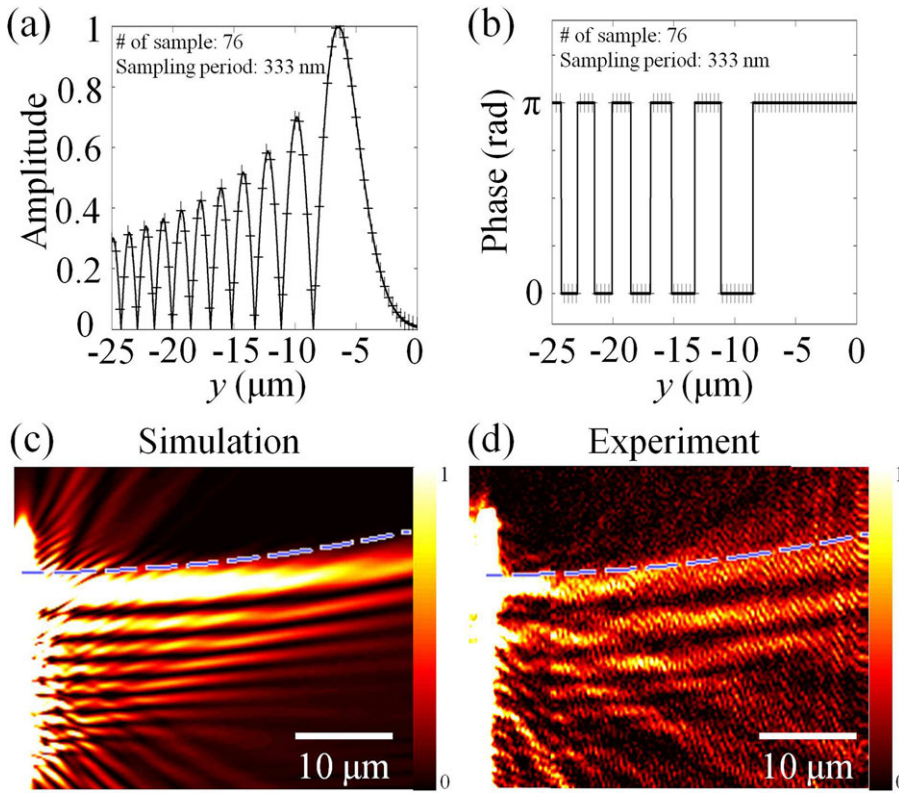


Figure 5 Airy complex-field profile expressed as Eq. (7) for (a) amplitude and (b) phase. Sampling locations are marked as '+'. Results for plasmonic Airy beam generation in (c) numerical simulation and (d) NSOM measurement. Blue dashed curves are the main lobe trajectory of the target Airy plasmon expressed as Eq. (8).

The function Airy is an Airy function defined in [9], y_0 is a half-width of the main lobe, and a is a parameter defining exponential apodization of the Airy plasmon profile.

Following the same procedure as in the previous section, we designed the tilted angles of double-lined nanoslit arrays. The sampling process is shown in Figs. 5a and 5b for amplitude and phase, respectively. The sampling range is from $y = -25 \mu\text{m}$ to $y = 0 \mu\text{m}$. The number of samples is 76, which determines the period of sampling as 333 nm. We determined the slit dimension to be $300 \text{ nm} \times 80 \text{ nm}$. Using calculations similar to those in the previous section, the coupling efficiency from free-space to the SPP wave for a $300 \text{ nm} \times 80 \text{ nm}$ slit dimension is calculated to be $\sim 12.5\%$. In this section, we select the polarization as RCP. Similar to the previous example, we determined appropriate tilted angles, ϑ_L and ϑ_R along the y -axis from the diagram shown in Fig. 2c. It is noteworthy that there is a degree of freedom for determining tilted angles. Nevertheless, we numerically confirmed that the SPP fields generated from these different sets of tilted angles create the identical intensity profile of an Airy plasmon (see supplementary material Part B).

4.2. Simulation and experimental result

We provide simulation and experimental results in Figs. 5c and d, respectively. The blue dashed line is the main lobe

trajectory of the target Airy plasmon that can be expressed as [8]

$$y = \frac{x^2}{4k_{\text{SPP}}^2 y_0^3}, \quad (8)$$

where k_{SPP} is the wave number of the SPP mode. We set the other geometrical parameters of the Airy plasmon as $y_0 = 1500 \text{ nm}$ and $a = 0.05$. The calculated beam trajectory is in good agreement with the simulation results, although the calculated structure has a limited sample range and discrete diffraction elements. The experimental results show some deviations from the blue dashed curves, showing the diffraction of the beam along the $+x$ -axis. Similar to the previous example, we conclude that these deviations arise from the imperfect fabrication of nanoslit arrays and the slightly oblique incidence of the light. In Figs. 5c and d, some unexpected lines appear interfering with the original Airy pattern. This is related to the SPP field generation in y -direction. In calculating the amplitude and phase of the generated SPPs from the nanoslit array, only SPPs propagating along the x -direction are considered [36] although the SPPs propagating along the y -direction from each nanoslit may exist. For example, if the tilted angle of the slit is 90° , the slit is aligned with the x -axis, which mainly generates SPPs along the y -direction. Hence, some unexpected lines are generated in the experiment and simulation. However, although these fields may change the beam profile near the nanoslit array, we expect that y -directional propagation of SPP cannot dominantly change the beam profile far from

the slit in the x -direction, therefore the Airy beam profile far from the slit is not significantly distorted.

In addition to the Airy-beam example, we also conducted a numerical calculation of one more example using the proposed method, namely, the generation of a cosine-Gaussian beam as an amplitude-only example. The result related to cosine-Gaussian beam generation can be found in the supplementary Part C, which emphasizes the generality of the proposed method.

5. Conclusion and outlook

In conclusion, we proposed a design method for the generation of a plasmonic complex field. A double-lined nanoslit array configuration, which generates a plasmonic complex field as pixel-by-pixel, is employed. The proposed nanoslits are double-lined with a constant period along the longitudinal axis. In addition, each nanoslit has its own tilted angle along the longitudinal axis. The amplitude of the SPP can be modeled as the angular difference between two nanoslits, whereas the phase is controlled by the offset rotation angle. We also provided both simulation and experimental results that confirm our design strategy. More specifically, various plasmonic caustic curves and Airy plasmons were generated. The proposed design mechanism is not restricted by these examples and it can be generally applied to any type of plasmonic complex field. We emphasize that these arbitrary plasmonic complex fields (e.g. nondiffracting beams, caustic curves and vortex beams) are widely used for optical trapping and guiding of microparticles along the arbitrary curves [41–43]. Moreover, this method can be used for holographic beam shaping [44, 45]. Therefore, our results could be used for potential applications in integrated optics, plasmonic beam shaping, and next-generation holography.

Supporting Information

Additional supporting information may be found in the online version of this article at the publisher's website.

Acknowledgements. This work was supported by the National Research Foundation of Korea funded by Korean government (MSIP) through the Creative Research Initiatives Program (Active Plasmonics Application Systems).

Received: 3 October 2015, **Revised:** 23 December 2015,

Accepted: 4 January 2016

Published online: 2 February 2016

Key words: Surface plasmon polaritons, metasurfaces, near-field generation, caustics, Airy beam.

References

- [1] S. Maier, *Plasmonics: Fundamentals and Applications* (Springer, NY, USA, 2007).
- [2] J. Heber, *Nature* **461**, 720–722 (2009).
- [3] M. L. Brongersma, and V. M. Shalaev, *Science* **328**, 440–441 (2010).
- [4] O. Brzobohatý, M. Šiler, J. Trojek, L. Chvátal, V. Karásek, A. Paták, Z. Pokorná, F. Mika, and P. Zemánek, *Sci. Rep.* **5**, 8106 (2015).
- [5] M. L. Juan, M. Righini, and R. Quidant, *Nature Photon.* **5**, 349–356 (2011).
- [6] M. Righini, A. S. Zelenina, C. Girard, and R. Quidant, *Nature Phys.* **3**, 477–480 (2007).
- [7] I. Epstein and A. Arie, *Phys. Rev. Lett.* **112**, 023903 (2014).
- [8] P. Zhang, S. Wang, Y. Liu, X. Yin, C. Lu, Z. Chen, and X. Zhang, *Opt. Lett.* **36**, 3191–3193 (2011).
- [9] A. Minovich, A. E. Klein, N. Janunts, T. Pertsch, D. N. Neshev, and Y. S. Kivshar, *Phys. Rev. Lett.* **107**, 116802 (2011).
- [10] L. Li, T. Li, S. M. Wang, C. Zhang, and S. N. Zhu, *Phys. Rev. Lett.* **107**, 126804 (2011).
- [11] F. Bleckmann, A. Minovich, J. Frohnhaus, D. N. Neshev, and S. Linden, *Opt. Lett.* **38**, 1443–1445 (2013).
- [12] J. Lin, J. Dellinger, P. Genevet, B. Cluzel, F. de Fornel, and F. Capasso, *Phys. Rev. Lett.* **109**, 093904 (2012).
- [13] A. E. Minovich, A. E. Klein, D. N. Neshev, T. Pertsch, Y. S. Kivshar and D. N. Christodoulides, *Laser Photon. Rev.* **8**, 221–232 (2014).
- [14] P. Genevet, J. Lin, M. A. Kats, and F. Capasso, *Nature Commun.* **3**, 1278 (2012).
- [15] D. Wintz, P. Genevet, A. Ambrosio, A. Woolf, and F. Capasso, *Nano Lett.* **15**, 3585–3589 (2015).
- [16] A. E. Cetin, A. F. Coskun, B. C. Galarreta, M. Huang, D. Herman, A. Ozcan, and H. Altug, *Light Sci. Appl.* **3**, e122 (2014).
- [17] A. G. Brolo, *Nature Photon.* **6**, 709–713 (2012).
- [18] H. Kim, J. Park, S.-W. Cho, S.-Y. Lee, M. Kang, and B. Lee, *Nano Lett.* **10**, 529–536 (2010).
- [19] Z. Fang, Q. Peng, W. Song, F. Hao, J. Wang, P. Nordlander, and X. Zhu, *Nano Lett.* **11**, 893–897 (2011).
- [20] Y. Gorodetski, A. Niv, V. Kleiner, and E. Hasman, *Phys. Rev. Lett.* **101**, 043903 (2008).
- [21] K. A. Bachman, J. J. Peltzer, P. D. Flammer, T. E. Furtak, R. T. Collins, and R. E. Hollingsworth, *Opt. Exp.* **20**, 1308–1319 (2012).
- [22] W.-H. Lee, *Appl. Opt.* **18**, 3661–3669 (1979).
- [23] I. Epstein and A. Arie, *Opt. Lett.* **39**, 3165–3168 (2014).
- [24] I. Epstein, Y. Lilach, and A. Arie, *J. Opt. Soc. Am. B* **31**, 1642–1647 (2014).
- [25] P. A. Huidobro, M. L. Nesterov, L. Martín-Moreno, and F. J. García-Vidal, *Nano Lett.* **10**, 1985–1990 (2010).
- [26] G. D. Valle and S. Longhi, *Phys. Rev. B* **82**, 153411 (2010).
- [27] T. Zentgraf, Y. Liu, M. H. Mikkelsen, J. Valentine, and X. Zhang, *Nature Nanotechnol.* **6**, 151–155 (2011).
- [28] A. B. Evlyukhin, S. I. Bozhevolnyi, A. L. Stepanov, and J. R. Krenn, *Appl. Phys. B* **84**, 29–34 (2006).
- [29] A. Drezet, D. Koller, A. Hohenau, A. Leitner, F. R. Aussenegg, and J. R. Krenn, *Nano Lett.* **7**, 1697–1700 (2007).
- [30] O. Avayu, I. Epstein, E. Eizner, and T. Ellenbogen, *Opt. Lett.* **40**, 1520–1523 (2015).
- [31] N. Yu, and F. Capasso, *Nature Mater.* **13**, 139–150 (2014).
- [32] N. Yu, F. Aieta, P. Genevet, M. A. Kats, Z. Gaburro, and F. Capasso, *Nano Lett.* **12**, 6328–6333 (2012).
- [33] S. Sun, Q. He, S. Xiao, Q. Xu, X. Li, and L. Zhou, *Nature Mater.* **11**, 426–431 (2012).

- [34] A. V. Kildishev, A. Boltasseva, and V. M. Shalaev, *Science* **339**, 1232009 (2013).
- [35] J. Lin, J. P. B. Mueller, Q. Wang, G. Yuan, N. Antoniou, X.-C. Yuan, and F. Capasso, *Science* **340**, 331–334 (2013).
- [36] S.-Y. Lee, K. Kim, S.-J. Kim, H. Park, K.-Y. Kim, and B. Lee, *Optica* **2**, 6–13 (2015).
- [37] S.-Y. Lee, S.-J. Kim, H. Kwon, and B. Lee, *IEEE Photon. Technol. Lett.* **27**, 705–708 (2015).
- [38] G. Spektor, A. David, B. Gjonaj, G. Bartal, and M. Orenstein, *Nano Lett.* **15**, 5739–5743 (2015).
- [39] S.-Y. Lee, K. Kim, G.-Y. Lee, and B. Lee, *Opt. Exp.* **23**, 15598–15607 (2015).
- [40] L. Froehly, F. Courvoisier, A. Mathis, M. Jacquot, L. Furfaro, R. Giust, P. A. Lacourt, and J. M. Dudley, *Opt. Exp.* **19**, 16455–16465 (2011).
- [41] D. G. Grier, *Nature* **424**, 810–816 (2003).
- [42] J. Arlt, V. Garces-Chavez, W. Sibbett, and K. Dholakia, *Opt. Commun.* **197**, 239–245 (2001).
- [43] V. Garces-Chavez, D. McGloin, H. Melville, W. Sibbett, and K. Dholakia, *Nature* **419**, 145–147 (2002).
- [44] M. Ozaki, J.-I. Kato, and S. Kawata, *Science* **332**, 218–220 (2011).
- [45] P. Genevet, J. Lin, M. A. Kats, and F. Capasso, *Nature Commun.* **3**, 1278 (2012).